sustainability

MDPI

Article

Study on Fluid–Solid Coupling Numerical Simulation and Early Warning of Weathered Granite Landslides Induced by Extreme Rainfall

Peng Yu [1,2], Honghua Liu [1,2], Hongbo Yu [1,2], Yongjian Xie [1,2], Yang Yu [1,2], Chenghao Zhu [3], Jie Dong [1,2,*] and Yong Guan [1,2,*]

1 Key Laboratory of Geological Safety of Coastal Urban Underground Space, Ministry of Natural Resources, Qingdao 266100, China; 13210276328@163.com (P.Y.)
2 Qingdao Geo-Engineering Surveying Institute, Qingdao 266100, China
3 Department of Environmental Science and Engineering, Ocean University of China, Qingdao 266100, China
* Correspondence: 13853286966@163.com (J.D.); qddkgy@163.com (Y.G.)

Abstract: Rainfall is the main factor inducing landslides. Clarifying rainfall-induced landslides' mechanisms and establishing adequate warning and prevention measures are crucial for regional disaster prevention and sustainable development. The weathering degree of fully weathered granite slopes is high, and the engineering mechanics property is poor, so it is easy to lose stability under extreme rainfall conditions. In this paper, the Fanling fully weathered granite landslide in Laoshan Scenic Spot in eastern China is taken as the research object, and the fluid–solid coupling landslide numerical model is established using ABAQUS 2022. The numerical simulation is carried out under five different rainfall intensity and time conditions, and the seepage field response, deformation response, and stability of the slope are analyzed. The research results indicate that (1) the fully weathered granite landslide in Fanling is a thrust-type landslide, and the response of horizontal deformation is greater than that of vertical deformation. (2) Compared with a long-term small rainstorm, a short-term heavy rainstorm is more harmful, and the slope is more prone to instability and damage. (3) The established unstable and under-stable rainfall warning curves for fully weathered granite landslides can provide a reference for the warning and prevention of similar regional landslides.

Keywords: weathered granite landslides; extreme rainfall; fluid–solid coupling; numerical simulation; rainfall warning curve

check for updates

Citation: Yu, P.; Liu, H.; Yu, H.; Xie, Y.; Yu, Y.; Zhu, C.; Dong, J.; Guan, Y. Study on Fluid–Solid Coupling Numerical Simulation and Early Warning of Weathered Granite Landslides Induced by Extreme Rainfall. *Sustainability* **2023**, *15*, 11738. https://doi.org/10.3390/su151511738

Academic Editor: Antonio Miguel Martínez-Graña

Received: 13 June 2023
Revised: 24 July 2023
Accepted: 28 July 2023
Published: 30 July 2023

1. Introduction

Landslides are one of the most common geological disasters. Under terrain, rainfall, and artificial unloading, the rock and soil on the slope break the original balance and slide along the weak surface. Due to the numerous mountainous areas in China, landslide disasters occur frequently. According to the Ministry of Natural Resources of China statistics [1], 5659 geological disasters occurred nationwide in 2022, resulting in a direct economic loss of CNY 1.5 billion. Among them, 3919 landslides, accounting for nearly two-thirds of the total, pose a significant threat to the safety of people's lives and property. In 2020, the State Council of China launched the first national geological disaster risk survey, which shifted its work philosophy from focusing on post-disaster relief to pre-disaster prevention, from reducing disaster losses to reducing disaster risks. In 2022, 905 geological disasters were successfully predicted nationwide, avoiding 7226 potential casualties due to the disaster [1]. Therefore, it is crucial to clarify the mechanism of landslide induction and develop adequate warning and prevention measures for geological disaster reduction.

In studying the mechanism and warning of rainfall-induced landslides, in addition to physical model experiments, numerical simulation is the most commonly used method [2]. Standard methods include the Finite Element Method [3], Difference Method [4], Discrete

Element Method [5], Material Point Method [6], Computational Fluid Dynamics [7], etc. Commonly used geological mechanics analysis and numerical simulation software include GeoStudio [8], RocScience [9], ABAQUS [10], FLAC3D [11], 3DEC [12], COMSOL [13], and so on. By combining finite element and extensive deformation analyses, Chen et al. [14] revealed the landslide mechanism from instability to ultimate flow failure. Research has found that the increase in pore water pressure caused by rainfall leads to the formation of plastic shear bands, at which point slope failure begins. The subsequent flow-like deformation is caused by the strain-softening effect related to enormous strains. Yu et al. [15] simulated the evolution trend of the water head, saturation zone, transition zone, and humid zone in the soil interlayer of the slope, deepening the understanding of the instantaneous infiltration of inclined soil interlayer rock slope and helping to evaluate the changes in slope stability during rainfall. Thomas et al. [16] proposed the transient rainfall infiltration and grid-based slope stability model (TRIGRS), which is more sensitive and reliable when calculating the safety factor and pore water pressure during and after rainfall. They can accurately predict 67% of landslides in the Himalayas region. Bilal et al. [17] used 3D coupled discrete metamodeling and computational fluid dynamics (CFD) methods to conduct a dynamic analysis of the Fuquan landslide and its shock wave. Jéssica [18] combines the three-dimensional variable saturated flow solver with the infinite slope stability method to calculate the statistical distribution of the safety factor and pore pressure at the soil bedrock interface.

Related scholars have also conducted numerical simulations of landslides induced by the combined effects of rainfall and other factors. Laxman et al. [19] conducted a transient hydromechanical analysis of the Bianjiazhai landslide, analyzing the impact of rainfall and reservoir water level fluctuations on the slope. The study found that when the reservoir suddenly draws water from a large area, the stability of the slope will be significantly reduced. Xu et al. [20] studied the seepage and deformation of unsaturated slopes during rainfall after an earthquake. They found that earthquakes significantly affect the sliding surface of slopes affected by rains, leading to more severe landslides. Li et al. [21] combined the SLOPE Permeability Distribution Equilibrium (SLIDE) model with the Landscape Evolution Model (CAESAR Lisflood) to establish the interaction mechanism between the "Rainfall Landslide Mountain Flood" disaster chain and the dynamic changing environment in mountainous areas, effectively predicting the susceptibility of landslides under extreme rainfall in the Wenchuan earthquake area. Wang et al. [22] used the Monte Carlo simulation method to establish a reverse analysis method to identify landslide events caused by typhoons and excessive rainfall. They defined the threshold for exceeding each region by using corresponding cumulative rain. Hao et al. [23] integrated rainfall infiltration boundary conditions and Mohr–Coulomb criteria into the thermal-hydraulic mechanical (THM) model and analyzed a landslide case in the Permafrost region. In recent years, relevant scholars have begun to study the relationship between landslides and rainfall distribution [24]. Dou et al. [25] used the typical rainfall intensity duration (I-D) threshold model as the research object, combined with China's geographical characteristics and 20-year average annual rainfall, to characterize the spatial distribution of rain-induced landslide warning thresholds in China. Liu and Wang [26] used the bivariate distribution of rainfall intensity and duration to solve the annual probability of slope failure caused by specific slope rainfall. In addition, AI and machine learning methods have also been applied to the numerical analysis of landslides. For example, Wei et al. [27] studied the safety factor of slopes under different groundwater levels. They determined the rainfall threshold using the genetic algorithm back-propagation neural network (GA-BPNN) method and the genetic algorithm support vector machine (GA-SVM) method. Mandal et al. [28] combine ABC artificial bee colony, WT wavelet transform, and KELM Extreme learning machine algorithm based on the kernel to build a landslide displacement prediction program. Novellino et al. [29] have established a landslide risk assessment model based on deep learning and benchmark machine learning algorithms. Wang et al. [30] used artificial intelligence methods such as GIS-based Bayesian networks, holding trees, and logistic model trees to evaluate landslide sensitivity. Landslide susceptibility prediction is a prerequisite for preventing and reducing landslide hazards. Skrzypczak et al. [31] conducted a landslide susceptibility study using the Hellwig method in the Carpathian region of southern Poland.

Due to the high degree of weathering and soft rock and soil strength, fully weathered granite slopes are prone to instability under extreme rainfall conditions. In previous studies, the author has conducted three sets of large-scale physical model tests (Figure 1) on the fully weathered granite landslide in Fanling under different rainfall conditions and preliminarily summarized the mechanism and failure process of rainfall-induced fully weathered granite landslide [32]. This paper is a follow-up study. Based on the prototype landslide data and physical model test results, a fluid–solid coupling numerical model is constructed to analyze further the impact of rainfall intensity and time on the stability of completely weathered granite. The research results guide disaster prevention, mitigation, and sustainable environmental development in similar regions.

Figure 1. Large-scale physical model test of Fanling landslide.

2. Characteristics of the Landslide

The Fanling landslide is located in the Laoshan Scenic Area of Qingdao, eastern China, with a central longitude and latitude of $120^{\circ}40'49.31''$ E and $36^{\circ}50'50.11''$ N (Figure 2). The area has many mountain ranges, mainly composed of hard block-like intrusive rock subregion (Figure 3). The granite has a high degree of weathering. Rainfall is concentrated in the flood season from June to August. According to the analysis of geological disasters, the time pattern of geological disasters in the study area is roughly the same as that of rainfall, generally occurring within three days after a heavy rainfall process or the end of rains. Rainfall, especially extreme rainfall, is one of the main factors causing geological disasters in the area.

Affected by heavy rainfall, the slope of Fanling collapsed in August 2007 and July 2020, respectively, resulting in one community resident's death and the road's destruction. When the landslide occurred on 22 July 2020, a single-day rainfall of 175.96 mm produced a typical rainfall-induced landslide (Figure 4). According to the analysis of field survey data, the Fanling landslide belongs to the ancient landslide of Quaternary and the modern loose accumulation layer. It is a soil-like landslide with a soft sliding surface, bulge at the front edge, obvious tension crack at the rear edge, etc. The failure mode of the sliding surface in fully weathered granite is thrust-type broken line sliding failure. At 175~228 m long, approximately 65~85 m wide, with a plan area of roughly 1.95×104 m^2, an average thickness of 12 m, and a volume of roughly 23.4×104 m^3, it is a medium-sized landslide. The leading edge elevation is 3–5 m, and the distance from the sea surface is 5–10 m; the rear edge elevation is 55–85 m, and the length along the highway is 290 m. The overall slope of the landslide is relatively steep, with an average gradient of 23°, and both the slope direction and the landslide direction are 130–140°. The rear edge of the landslide is the boundary between the bedrock and the Quaternary system, and the shear outlet is the residual slope boundary.

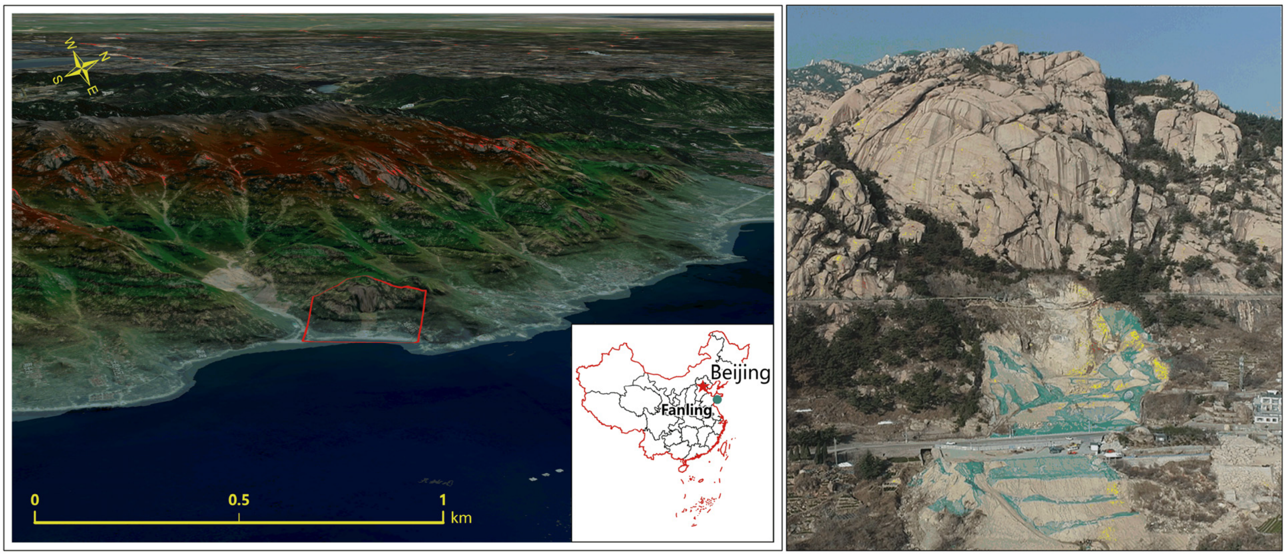

Figure 2. Location of Fanling landslide.

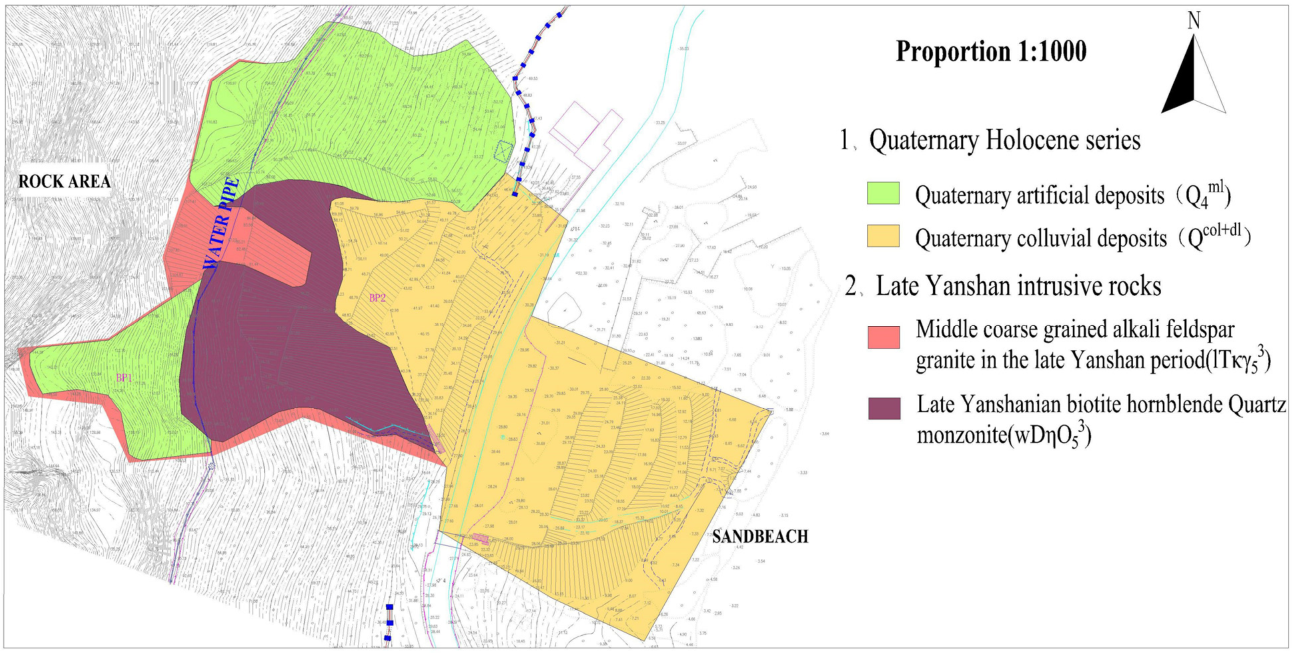

Figure 3. Geologic map of Fanling landslide.

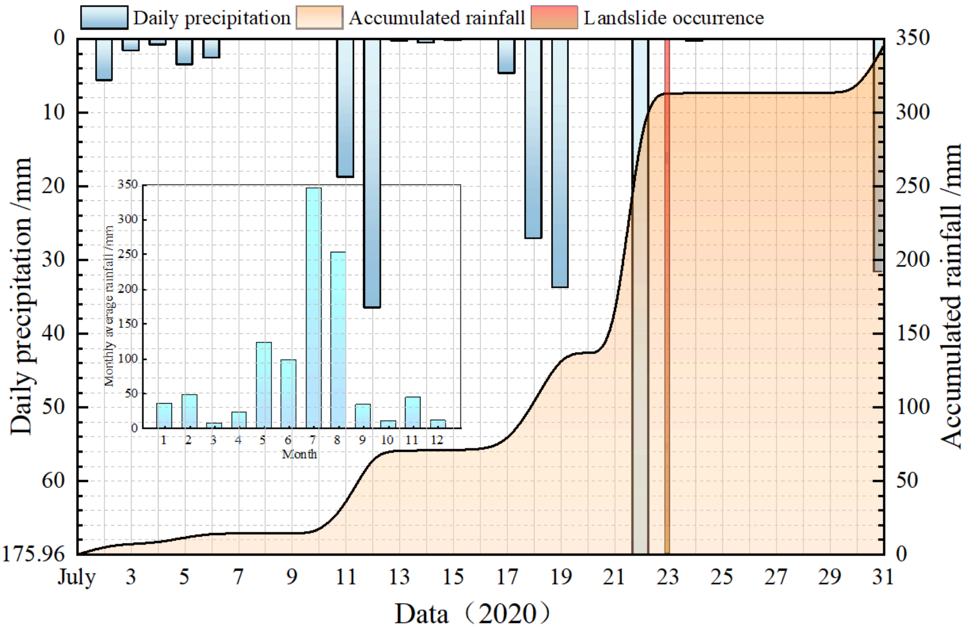

Figure 4. Rainfall time history of Fanling landslide in 2020.

3. Numerical Simulation

3.1. Simulation Method

Using ABAQUS software, Finite Element Simulation was conducted on slopes under different rainfall conditions. Considering that the underground seepage caused by rainwater is included in the model, the fluid/displacement unit in ABAQUS software can be used to directly couple the stress field and seepage field in the soil, and the strength reduction method is used to conduct numerical simulation calculation in the ground (Figure 5). The slope stability is analyzed according to the safety factor, plastic deformation range, and displacement.

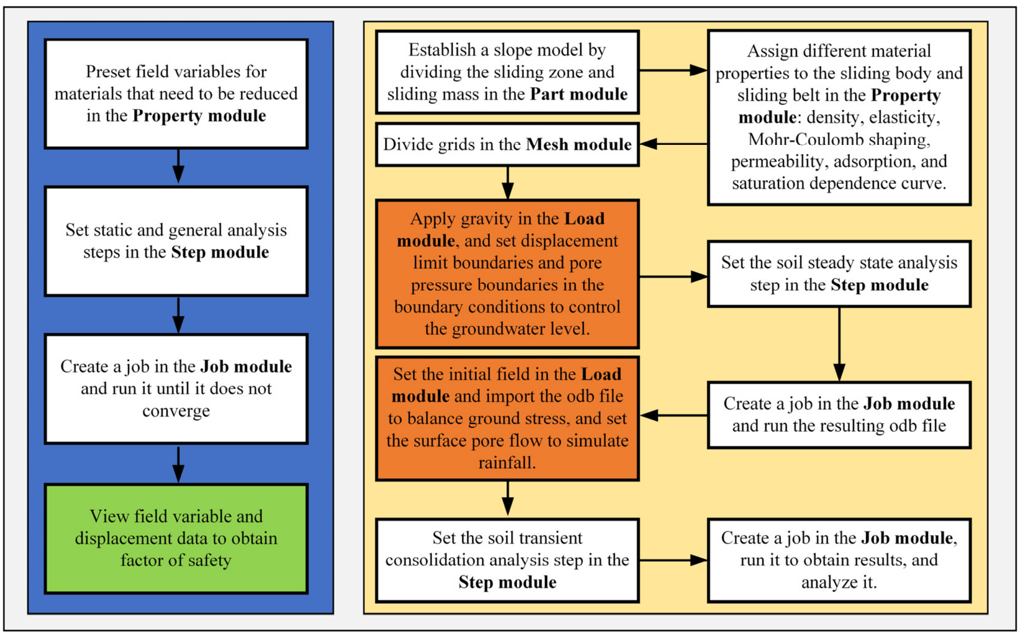

Figure 5. Numerical simulation process.

3.2. Modeling

According to the survey report data of the Fanling landslide [32], 3D rainfall fluid–solid coupling modeling [33,34] of the main sliding surface of the landslide is carried out. The geological profile is shown in Figure 6. After on-site exploration and drilling sampling, it was found that the lithological characteristics of the weathered layer and the weakly weathered layer are not significantly different, and their water permeability is extremely poor. The sliding interface is located at the geological interface between the completely weathered layer and the weathered layer, and there is no abnormal movement in the lower strata. Groundwater also flows along this interface. Considering that there is no effect on the stress field and seepage field, we simplified the model by using surface residual soil and completely weathered rock layers (sandy soil properties) as sliding mass (soil layers) and weathered and weakly weathered layers as sliding bed (rock layers). The slope model and material assignment are shown in Table 1. The model's overall length is 240 m, height is 85 m, width is 2.4 m, slope height is 54 m, and the foot of the slope β = 20.43°; the sliding body size is the same as the main screen profile.

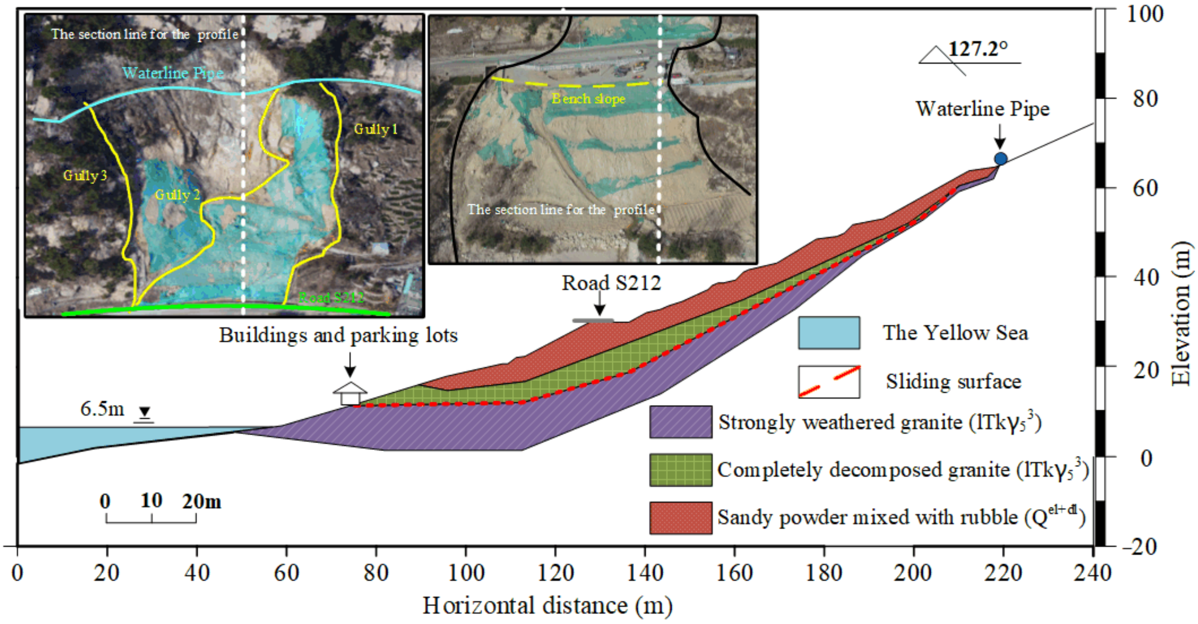

Figure 6. Geological profile of Fanling landslide.

Table 1. Model material parameters.

	Soil Weight (KN/m^3)	Elastic Modulus (kPa)	Poisson's Ratio	Internal Friction Angle (°)	Cohesive Force (kPa)	Permeability Coefficient (mm/h)
Sliding mass	19	50,000	0.25	20	25	0.08
Sliding bed	26	1,000,000	0.2	37	1000	0.00001

Firstly, mesh the model. The mesh element type is C3D8P, which is an eight-node hexahedron element. Both displacement and pore pressure are set in a three-dimensional linear manner. Finally, the model was structured with a total of 11,192 units.

Apply the *X*-direction displacement constraint in the *X*-direction, the *Z*-direction displacement constraint in the *Z*-direction, and *XYZ* three-dimensional displacement constraint at the bottom. Apply pore pressure boundaries on both interface sides in the *X* direction to simulate the pore water pressure and saturation under the original working conditions. The self-weight and hydrostatic pressure on both sides of the immersed water affect the entire model. Apply surface pore flow on the surface of the model sliding body to simulate rainfall. Set up five monitoring points from the foot of the slope to the top of the slope to extract simulated data for analysis (Figure 7). The displacement (horizontal and vertical displacement), pore pressure, saturation, and equivalent plastic strain data for each working condition can be automatically extracted by the ABAQUS output module.

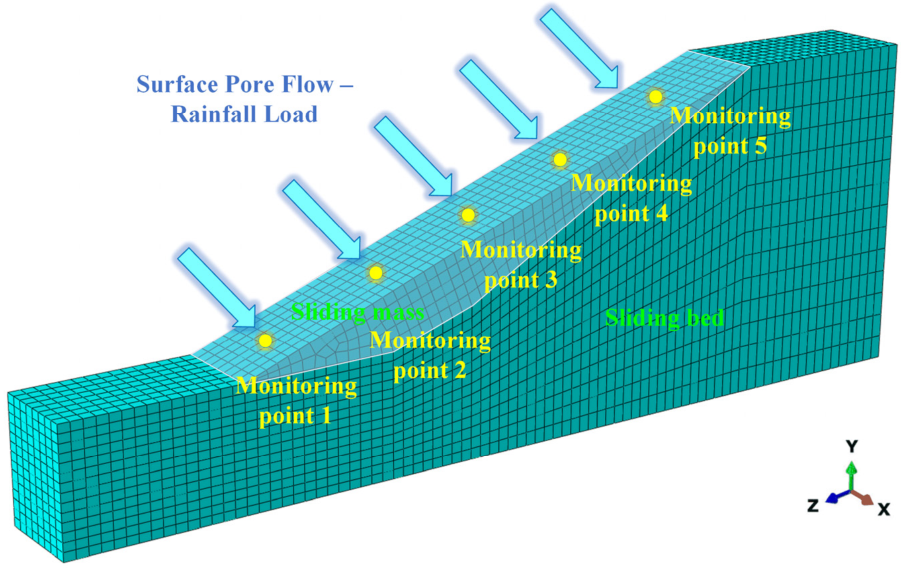

Figure 7. Model diagram.

In combination with local rainfall data and physical model test settings, five different rainfall conditions are set (Table 2): fifty-year return period (N1), rainstorm (N2), heavy rainstorm (N3), continuous rainstorm (N4), and long-term rainstorm (N5).

Table 2. Simulated working conditions.

Group	Rainfall Intensity (mm/h)	Rainfall Time (h)
N1	32	24
N2	20	24
N3	10	24
N4	20	48
N5	20	72

3.3. Grid Size

We carried out the grid-independence analysis using four mesh types (0.75, 1, 1.25, 1.5) with different cell numbers. Crucial variables most engineers are interested in are pore pressure and displacement. As shown in Figures 8 and 9, it is clear that there is no distinguishable deviation among the results of the four meshes. In this regard, we selected grid 1 (Figures 8b and 9b) for further investigations.

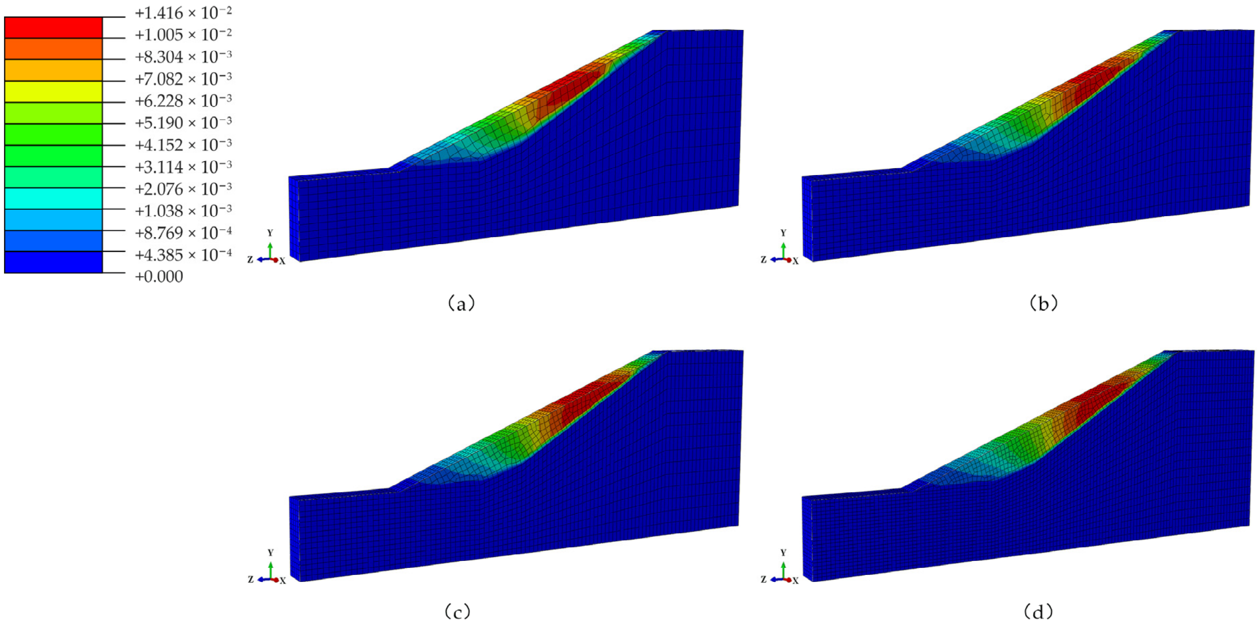

Figure 8. Distribution nephogram of displacement (**a**) 0.75; (**b**) 1; (**c**) 1.25; (**d**) 1.5.

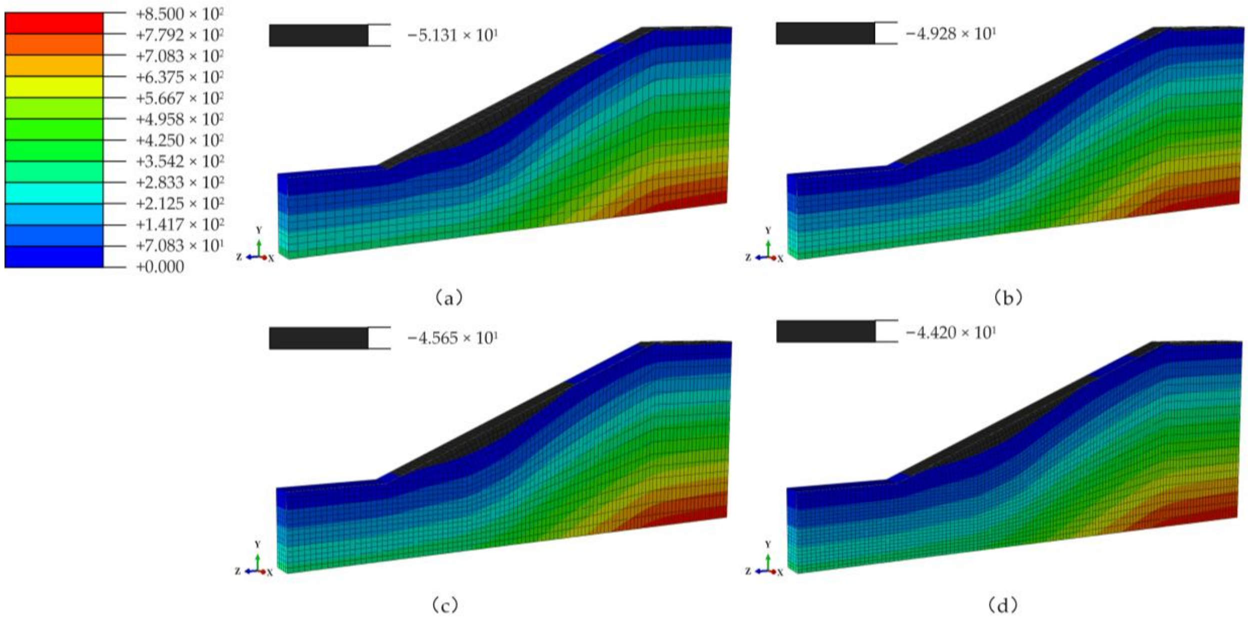

Figure 9. Distribution nephogram of pore pressure (**a**) 0.75; (**b**) 1; (**c**) 1.25; (**d**) 1.5.

4. Result and Analysis

4.1. Response of Seepage Field

The surface with zero pore pressure is the phreatic surface of groundwater. Since the sliding bed, in this case, is granite with a low weathering degree, its permeability tends to be zero, and only the bedrock fissure water does not conform to Darcy's law [35,36]; it is considered that the phreatic surface of groundwater is the junction of granite sliding bed and completely weathered rock sliding body [37,38]. The granite sliding bed part is considered saturated. Figure 10 shows the distribution of pore hydraulic pressure in slopes under different rainfall conditions. As the slope deepens, the pore pressure shows a decreasing trend, with the highest pore pressure in the lower part of the slope.

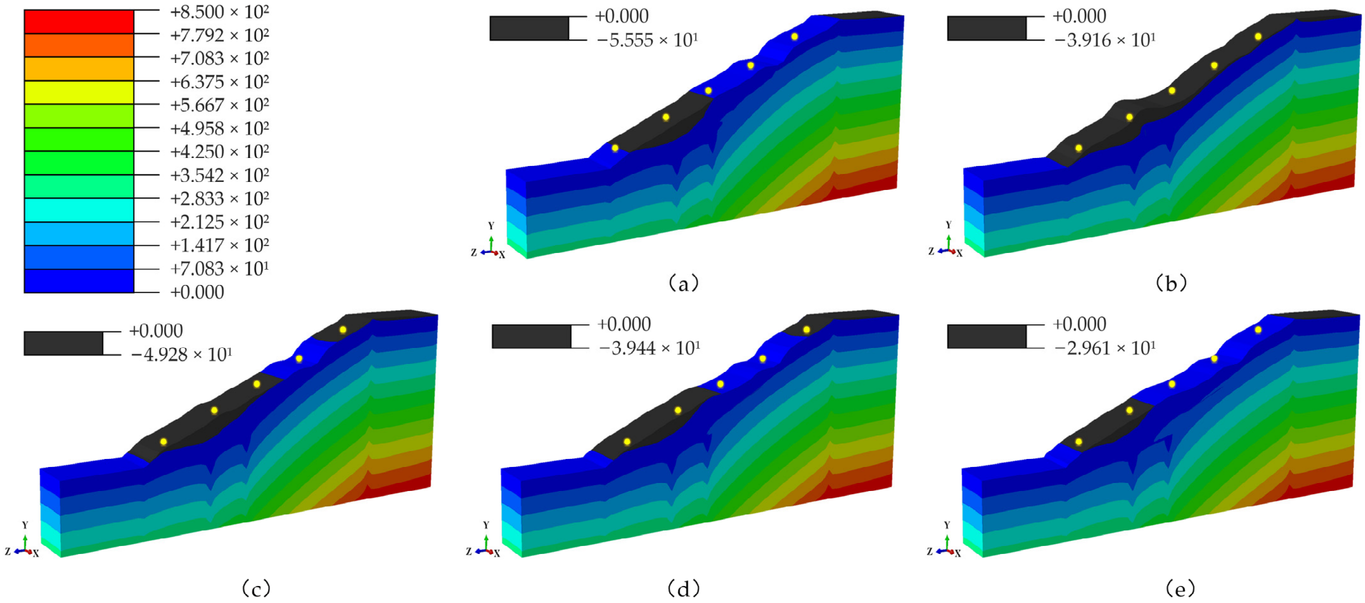

Figure 10. Distribution nephogram of pore pressure (**a**) N1; (**b**) N3; (**c**) N2; (**d**) N4; (**e**) N5.

Figure 11 shows the saturation distribution nephogram of the slope under different rainfall conditions. As rainfall conditions change, the saturated area of the slope exhibits significant movement and transitions. The intensity and time of rainfall will significantly impact the location of the groundwater infiltration surface on the slope. At N1, the groundwater infiltration surface has already approached the surface at most of the sliding bodies; at N2, the groundwater infiltration surface only becomes characterized at the thin sliding mass at the top of the slope; at N3, the groundwater infiltration surface shows little change compared to before rainfall. At N4, the groundwater infiltration surface only approaches the surface at the thinner part of the slope top sliding mass; at N5, the groundwater infiltration surface has already closed the surface at most of the sliding bodies. After conversion, when there is no rainfall, the boundary pore pressure of the slope soil is 0 kPa (calculated as −59.68 kPa). As the rainfall intensity increases to 32 mm/h (N1), 20 mm/h (N2), and 10 mm/h (N3), the boundary pore pressure increases to 20.52 kPa, 10.4 kPa, and 4.46 kPa, respectively. (The calculated values are −39.16 kPa, −49.28 kPa, and −55.22 kPa.) When the rainfall time increases to 48 h (N4) and 72 h (N5), the boundary pore pressure of the slope also increases to 20.24 kPa and 30.07 kPa, respectively. (The calculated values are −39.44 kPa and −29.61 kPa.)

Extract simulation results in data to draw a time history map of pore pressure changes (Figure 12). The saturation line inside the slope gradually rises with the increase in rainfall intensity and time, and the pore pressure at each monitoring point inside the slope also gradually increases. This indicates that slope saturation is positively correlated with rainfall intensity/time.

Under the same rainfall intensity, the pore pressure values of monitoring points at different positions on the slope are different, and their response to changes varies with the duration of rainfall. The thicker the completely weathered granite layer below the measuring point, the smaller its pore pressure value, and its growth trend is similar to the increase in rainfall intensity. Taking N5 as an example (Figure 12d), the monitoring point at the top of the slope has a faster increase in pore pressure. This is because the fully weathered rock layer at the top of the slope is relatively thin, and the groundwater infiltration surface increases rapidly. After about 18 h of rainfall, the pore pressure at monitoring points 4 and 5 at the top of the slope suddenly increased significantly; after about 31 h of rain, there was a significant increase in pore pressure at monitoring point 3, indicating that the groundwater infiltration surface was already higher than that of the monitoring point; the constant increase in pore pressure at monitoring point 1 and monitoring point 2 indicates that the groundwater infiltration surface will not be higher than this monitoring point under this working condition.

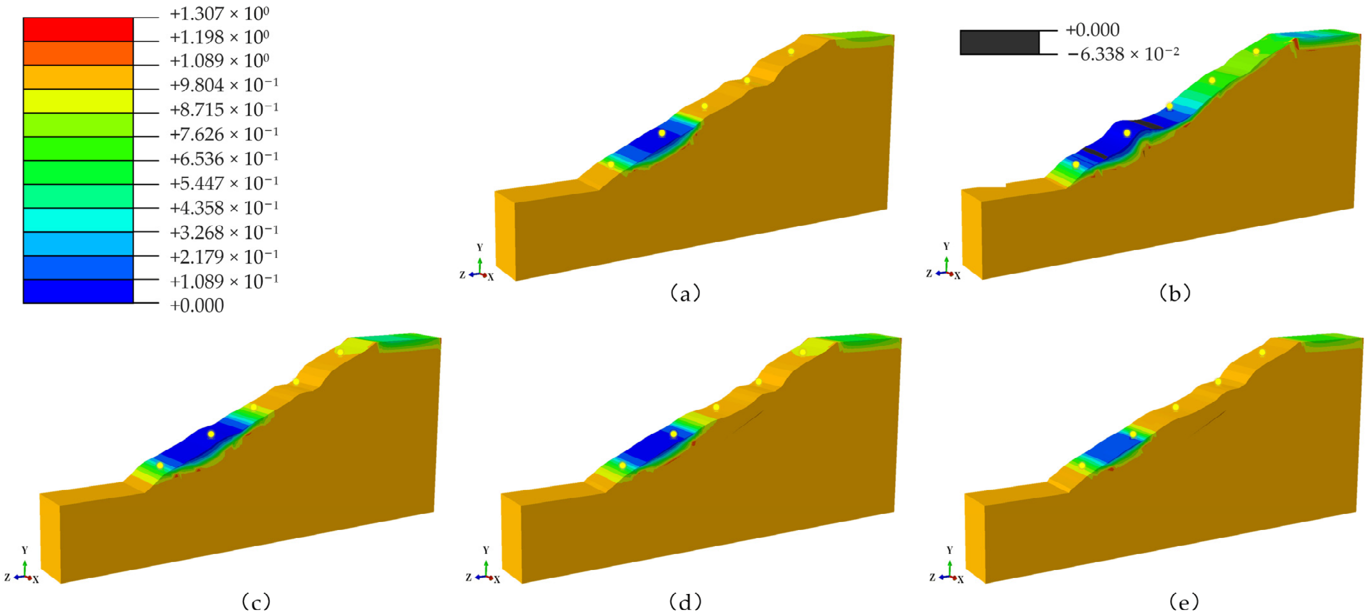

Figure 11. Distribution nephogram of saturation (**a**) N1; (**b**) N3; (**c**) N2; (**d**) N4; (**e**) N5.

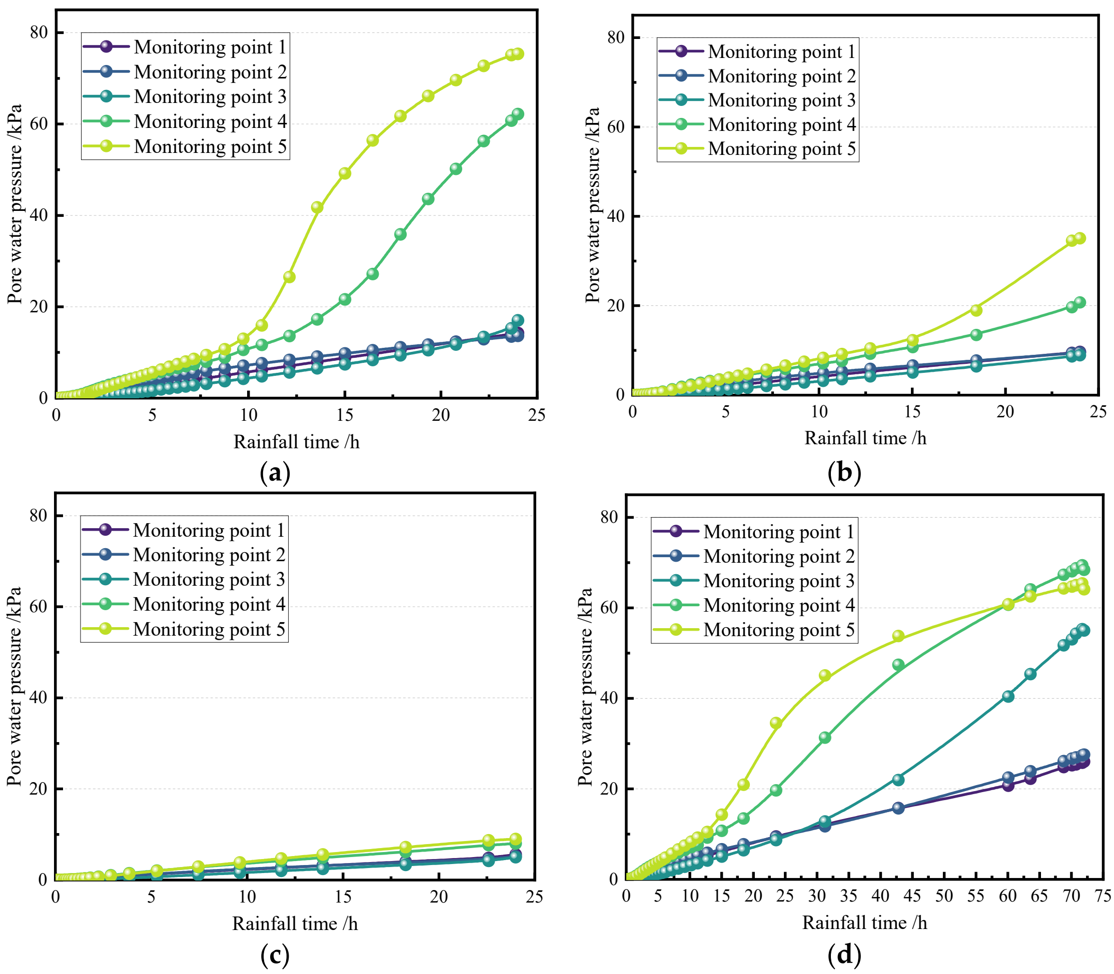

Figure 12. Slope pore pressure–time response diagram (**a**) N1; (**b**) N2; (**c**) N3; (**d**) N5.

Under different rainfall intensity conditions, the rate of pore pressure increase at the same monitoring point is significantly different. After 11 h of rainfall, the pore pressure of monitoring points 4 and 5, located at the top of the slope, suddenly increased significantly, indicating that the groundwater infiltration surface was higher than that of the monitoring point. N2 only experienced this phenomenon after about 17 h of rainfall, while N3 did not, indicating that the rainfall intensity (20 mm/h) was insufficient to cause large-scale changes in pore water pressure, thus not inducing landslides.

4.2. Response to Deformation

The displacement cloud map under different rainfall conditions is shown in Figure 13. Under additional rainfall intensity/time, the development trend of soil displacement is different due to rainwater infiltration in the slope. In this example, soil displacement starts from the middle of the slope and gradually develops towards the top of the slope, and finally deformation occurs at the bottom of the slope. This means that the top of the slope undergoes deformation first, and it can be inferred that the landslide is a thrust-type landslide, which is consistent with the results of physical model tests [32].

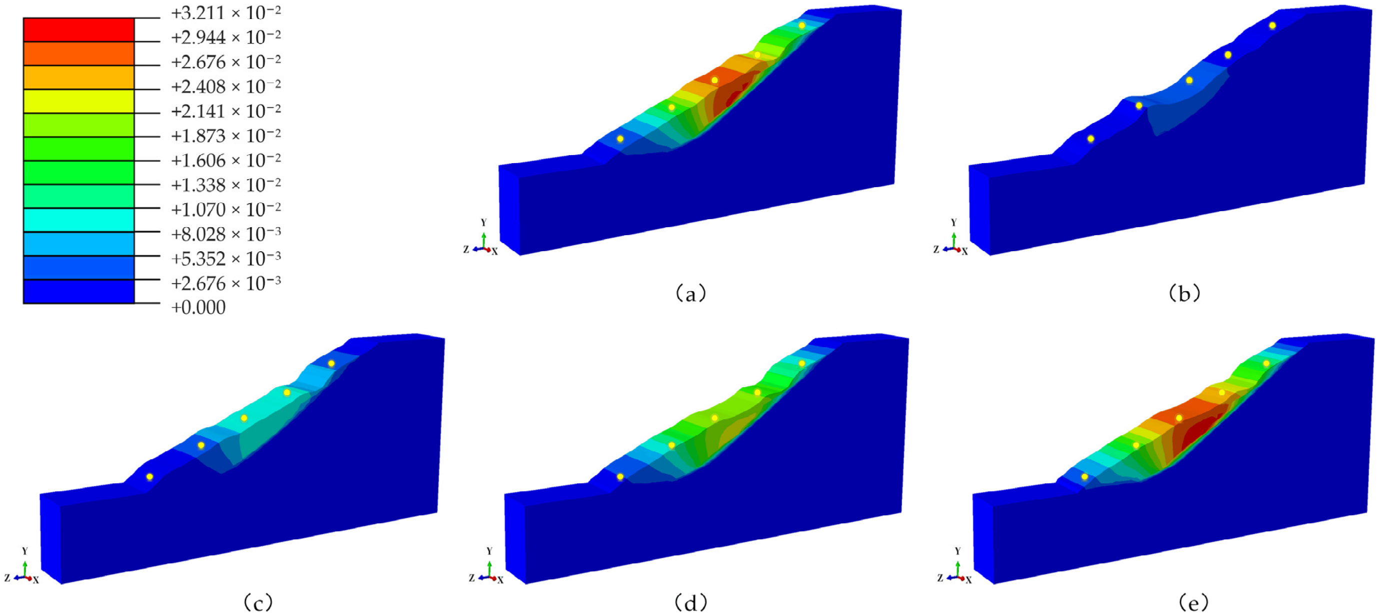

Figure 13. Distribution nephogram of displacement (**a**) N1; (**b**) N3; (**c**) N2; (**d**) N4; (**e**) N5.

The slope has different degrees of deformation under other rainfall conditions (Figure 14). The intensity and time of rainfall are positively correlated with the deformation of the slope. The slope displacement response of N1 is evident, with a significant deformation increment, and the maximum displacement is 3.051×10^{-2} m; in contrast, the maximum displacement of N2 and N3 slopes is 1.070, respectively, $\times$ 10^{-2} m and 5.085×10^{-3} m. For the same rainfall intensity, the slope displacement response of N5 is pronounced, with a significant deformation increment and a maximum displacement of 3.211×10^{-2} m, and the maximum displacement of N4 slope is 2.408×10^{-2} m (Figure 14d).

Furthermore, based on the horizontal and vertical displacement distribution nephogram under different rainfall conditions (Figures 15 and 16), the N1 operating condition data were extracted. The horizontal and vertical displacement time history maps were drawn (Figure 17a). Monitoring point 4, the point with the most significant displacement scale under all working conditions, separately extracted the horizontal and vertical displacements under different conditions (Figure 17b).

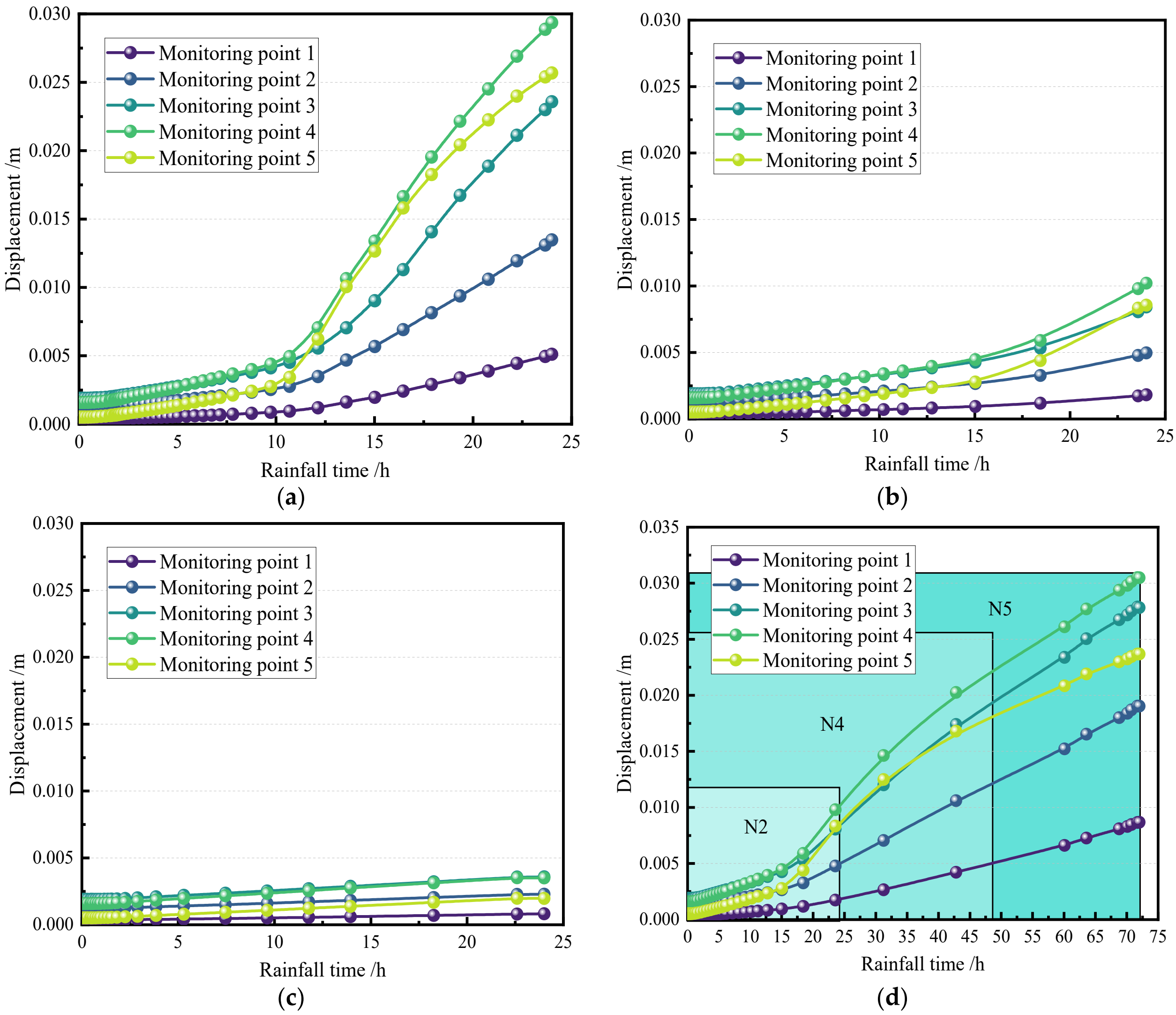

Figure 14. Slope displacement–time response diagram (**a**) N1; (**b**) N2; (**c**) N3; (**d**) N5.

Under extreme rainfall (N1), the slope response to horizontal deformation is more significant than that to vertical deformation at monitoring points with high displacement sensitivity. The displacement in both directions has undergone two processes: slow and rapid growth. After 18–19 h of rainfall, the displacement response of various slope parts rapidly increases, and the displacement at the top of the slope changes quickly. The vertical displacement response will lag slightly behind the horizontal displacement, and the response amplitude of each point on the slope is relatively large. The vertical displacement of monitoring points 3, 4, and 5 increases rapidly and then tends to flatten out.

As the rainfall intensity increases, the inflection points of the displacement change rates in both directions of advance. Under N1 conditions, the stress field response of the slope is evident, and the displacement is large. When rainfall lasts for 12–13 h, the displacement response of various slope parts increases significantly, and the displacement scale at the top of the slope is more significant than that at the bottom. Under the conditions of N2 and N3, during rainfall of 18–19 h, the displacement response of various parts of the slope increases, and the difference in displacement scale among monitoring points is not significant.

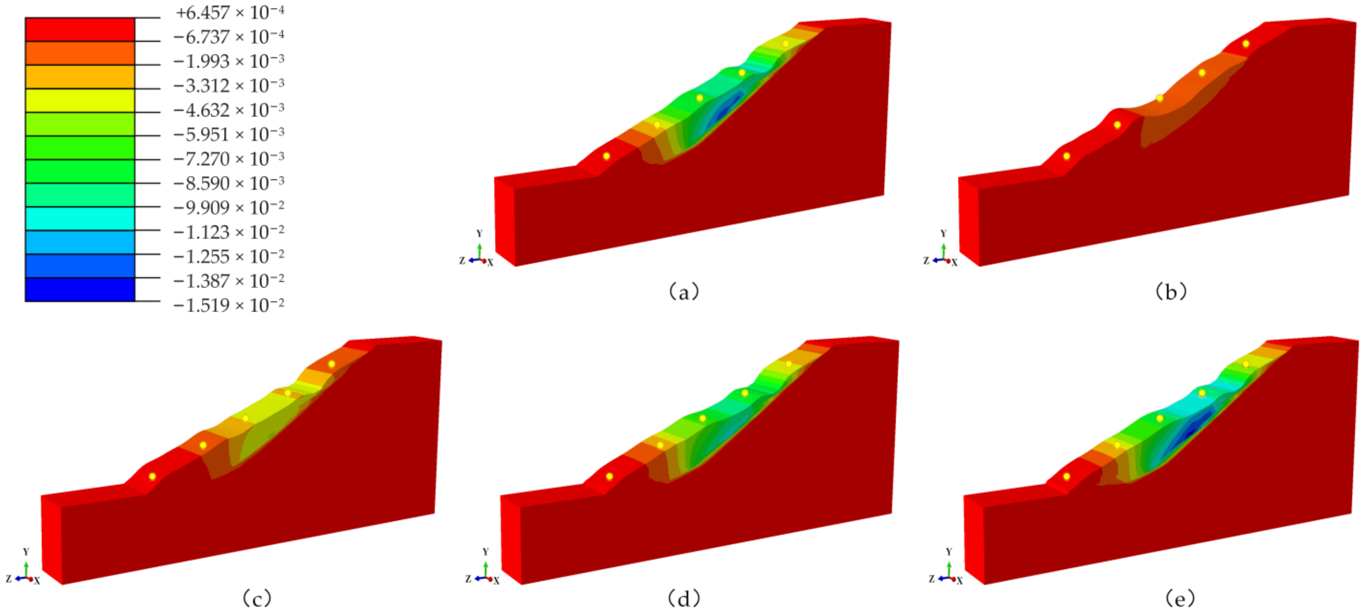

Figure 15. Vertical distribution nephogram of displacement (**a**) N1; (**b**) N3; (**c**) N2; (**d**) N4; (**e**) N5.

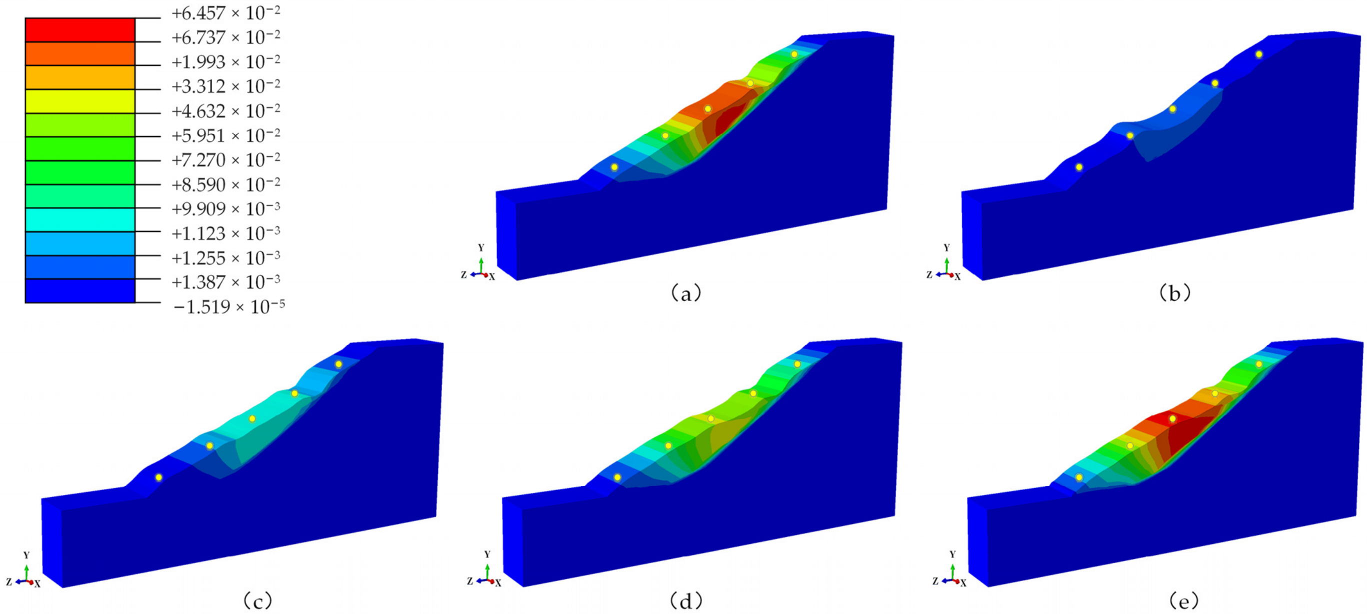

Figure 16. Horizontal distribution nephogram of displacement (**a**) N1; (**b**) N3; (**c**) N2; (**d**) N4; (**e**) N5.

4.3. Slope Stability

Table 3 shows the slope safety factor under different rainfall conditions. During the landslide process, its safety factor gradually decreases with increased rainfall intensity/time.

Table 3. Safety factor of slope.

Group	N1	N2	N3	N4	N5
Safety factor	1.168	1.378	1.495	1.214	1.126

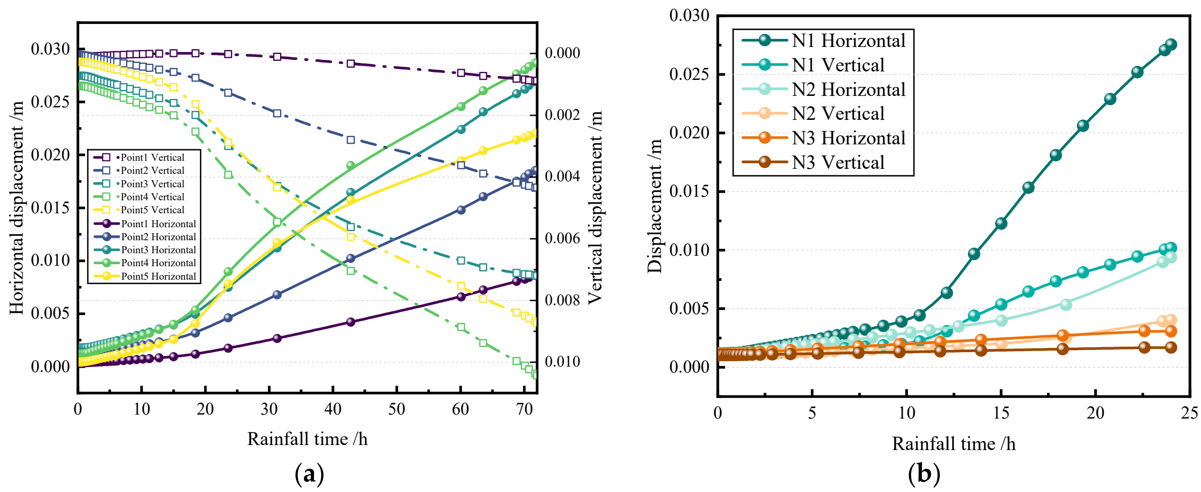

Figure 17. Horizontal and vertical displacement response diagram (**a**) N1; (**b**) Point 4.

When a slope experiences instability, the development of its plastic strain zone varies under different rainfall conditions (Figure 18). When there is no rainfall, the plastic strain caused by groundwater is minimal and can be ignored. However, as the rainfall intensity/time increases, the maximum plastic strain of the slope also increases. When the rainfall intensity is 32 mm/h, 20 mm/h, and 10 mm/h, the maximum plastic deformation of the slope is 3.689, respectively, $\times 10^{-2}$ (N1), 1.537 $\times$ 10^{-2} (N2) and 9.224 $\times$ 10^{-3} (N3). When the rainfall duration is 48 h (N4) and 72 h (N5), the maximum plastic deformation of the slope is 2.572 $\times$ 10^{-2} and 3.859 $\times$ 10^{-2}, respectively.

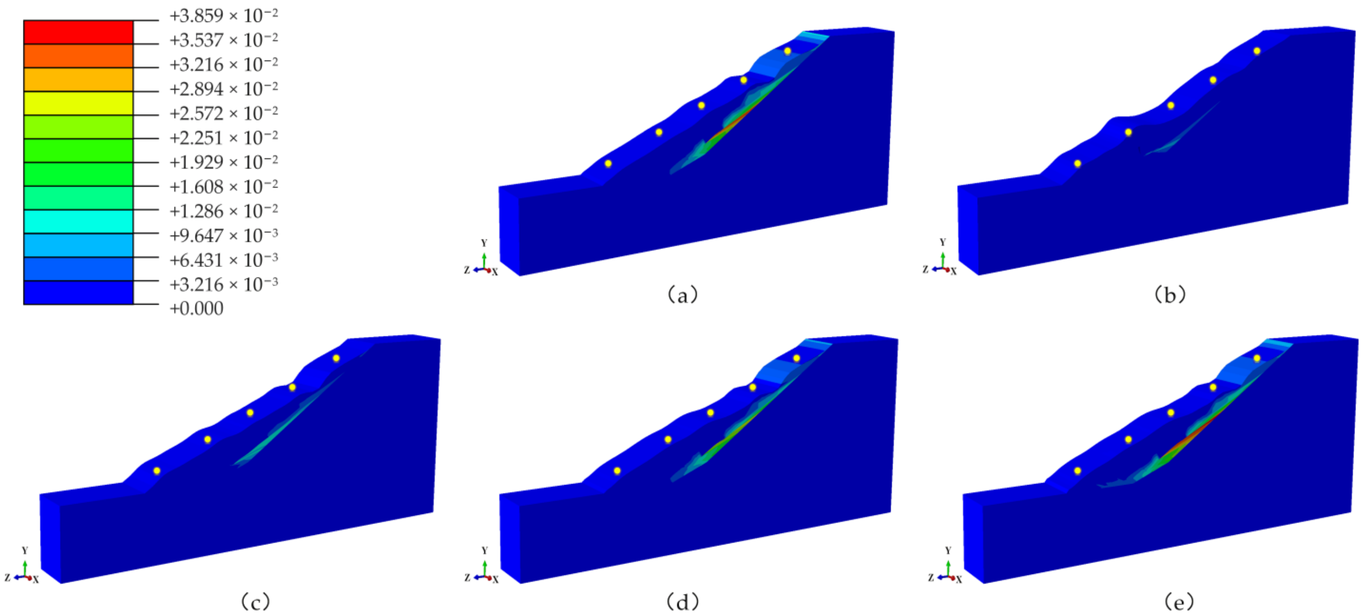

Figure 18. Distribution nephogram of equivalent plastic strain (**a**) N1; (**b**) N3; (**c**) N2; (**d**) N4; (**e**) N5.

Different from the plastic strain zone generated from the foot of the slope to the end of the slope top in conventional landslides [37,38], in this example, the plastic strain zone is generated from the middle of the slope, expanding in both directions at the bottom and top of the slope, and expanding faster towards the top of the slope, indicating that deformation first occurred in the upper part of the slope and formed a continuous circular sliding surface with the top of the slope, thereby triggering the overall landslide. At maximum rainfall intensity (N1) and maximum rainfall time (N5), the continuity of the plastic zone of the slope is more significant.

4.4. Comprehensive Analysis

Figure 19 shows each monitoring point's pore water pressure and displacement response data under different rainfall conditions. From Figure 19b,d, it can be seen that there are significant differences in the displacement response caused by rainwater dynamics at different parts of the slope. The displacement response at the top of the landslide is more critical than other factors. Due to the differences in geotechnical characteristics, such as saturated moisture content and elastic modulus of soil, thin soil is more sensitive to the dynamic load response of rainfall than thick soil, and the elastic modulus value of soil is negatively correlated with the deformation response. The front edge of the landslide soil undergoes shear creep towards the free direction, resulting in the most significant displacement response at monitoring points 4 and 5. In contrast, other monitoring points have smaller answers. Based on the slope's stress situation and the landslide structure's geomorphic characteristics before returning to the mountain, it is determined that the landslide is a thrust-type landslide.

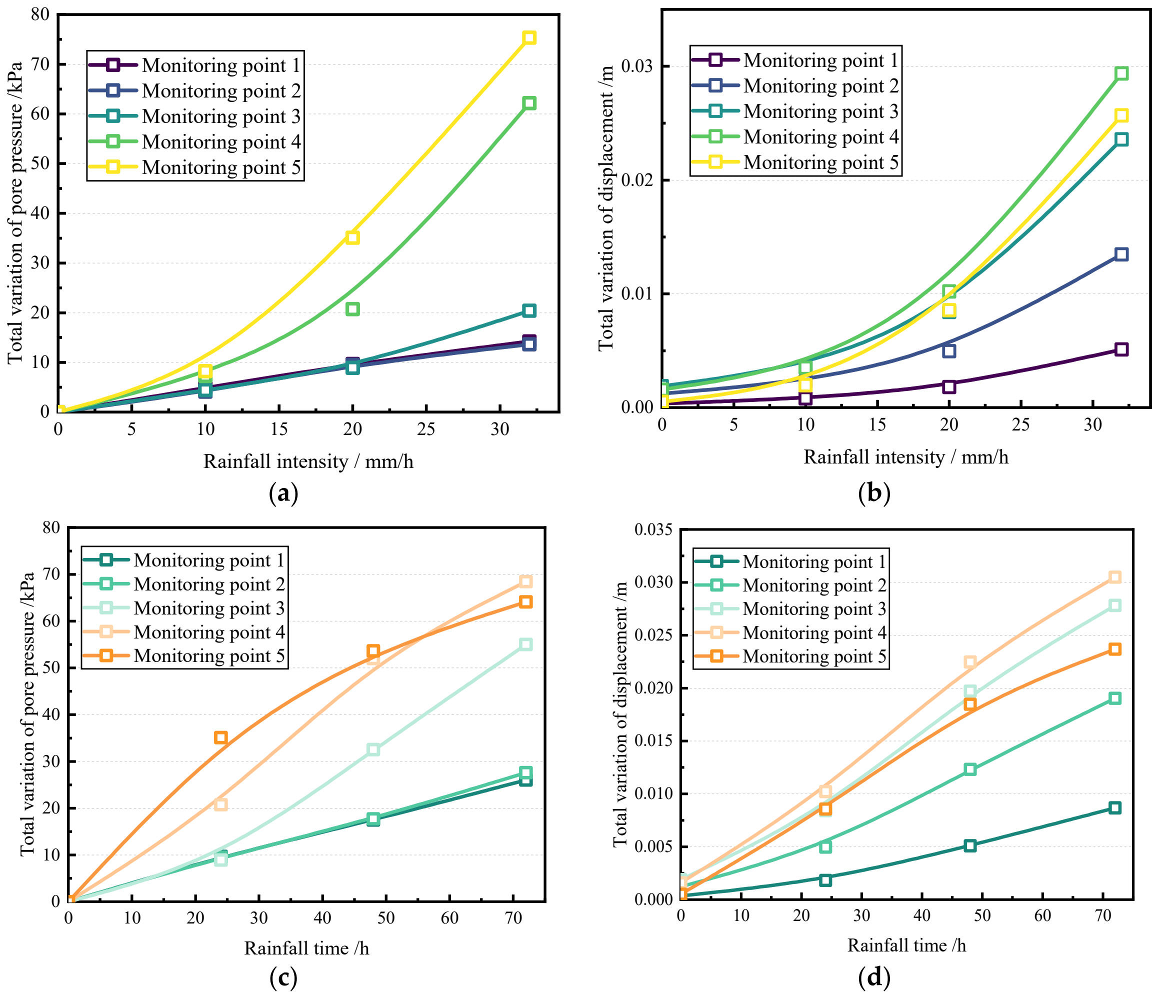

Figure 19. Final response of pore pressure and displacement (**a**,**b**) under different rainfall intensities; (**c**,**d**) under different rainfall times.

As the intensity of rainfall increases, the speed of slope damage also increases. Therefore, the pore pressure and displacement response rate values, i.e., the curve's curvature, show an increasing trend and are directly proportional to the rainfall intensity (Figure 19a,b). As the duration of rainfall increases, the slope angle of the curve, i.e., pore pressure and displacement response rate values, decreases (Figure 19c,d), indicating that the slope gradually tends to saturation, and the groundwater infiltration surface approaches the surface, possibly forming surface runoff. When the rainfall intensity is less than the permeability coefficient of completely weathered granite, the slope can fully absorb rainwater without generating slope runoff. The stronger the rainfall within a fixed time, the more water permeates the slope and the more significant the impact. The rainwater first invades the upper silty sand and residual soil layer and then infiltrates the fully weathered granite layer. At this time, the shear strength of the slope soil is reduced, the pore water pressure of both is changed, and the sliding force of the soil is significantly increased. It can be seen that water is the "lubricant" that induces landslides and is an essential condition for landslide induction.

Furthermore, extract the safety factor under different rainfall conditions (Figure 20). It can be seen from the curve that during the process, with the increase of rainfall intensity and duration, the slope stability and the safety factor when a landslide occurs show a decreasing trend. The reason is that the internal water storage capacity of the slope soil gradually increases with the increase in rainfall, leading to a gradual increase in the pore pressure and water content of the slope soil. Under the influence of the rainwater seepage flow field, the shear strength of the slope soil will gradually decrease, forming a "strength loss", thereby inducing slope collapse. When high-intensity concentrated rainfall occurs, rainwater infiltration will make the slope's shear failure more significant, thereby lowering slope stability.

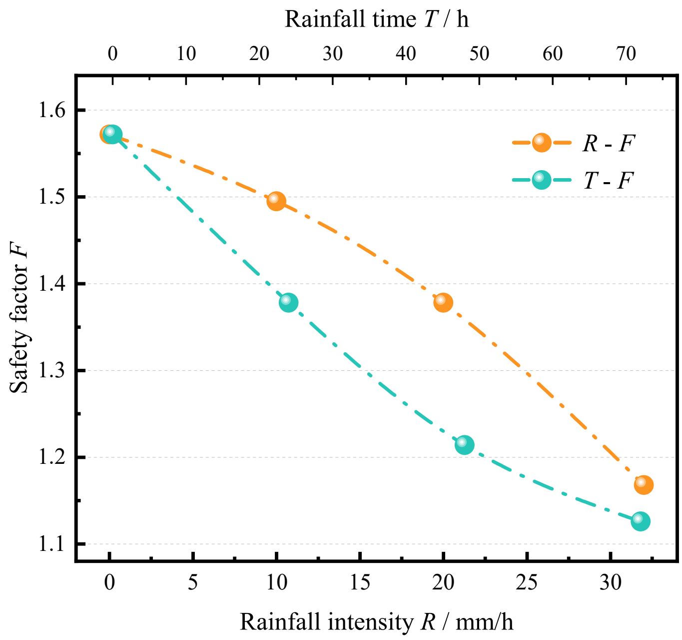

Figure 20. Comparison of safety factors.

Compared with the small long-term rainstorm with small rainfall intensity and long duration (N5), the short-term heavy rainstorm (N1) will make the response of pore pressure and displacement of the slope faster, the loss of safety factor of the slope is more, and the slope is more prone to instability and failure. This is because strong rainfall can cause substantial erosion and infiltration on the slope's soil, significantly weakening the strength of the slope, leading to a decrease in the stability of the slope, and causing severe landslides.

4.5. Early Warning

To quantitatively analyze the impact of rainfall on the stability of a completely weathered granite landslide, establish the rainfall warning curve of the landslide, and calculate the change curve of its landslide safety factor (*Fs*) as shown in Figure 21. According to the specification [39], when the landslide safety factor *Fs* < 1, the landslide is unstable. But when the landslide safety factor *Fs* < 1.1, the landslide displacement field begins to respond significantly, and there are specific errors in the numerical simulation. Therefore, the landslide safety factor *Fs* = 1.1 is the critical value of under-stable, and the landslide safety factor $Fs = 1$ is the critical value of unstable. When the landslide safety factor $Fs < 1.1$, it is considered that the slope has reached an under-stable state, and a landslide begins to occur; When the landslide safety factor $Fs < 1$, it is believed that the slope has reached the unstable state, and the landslide has overall instability.

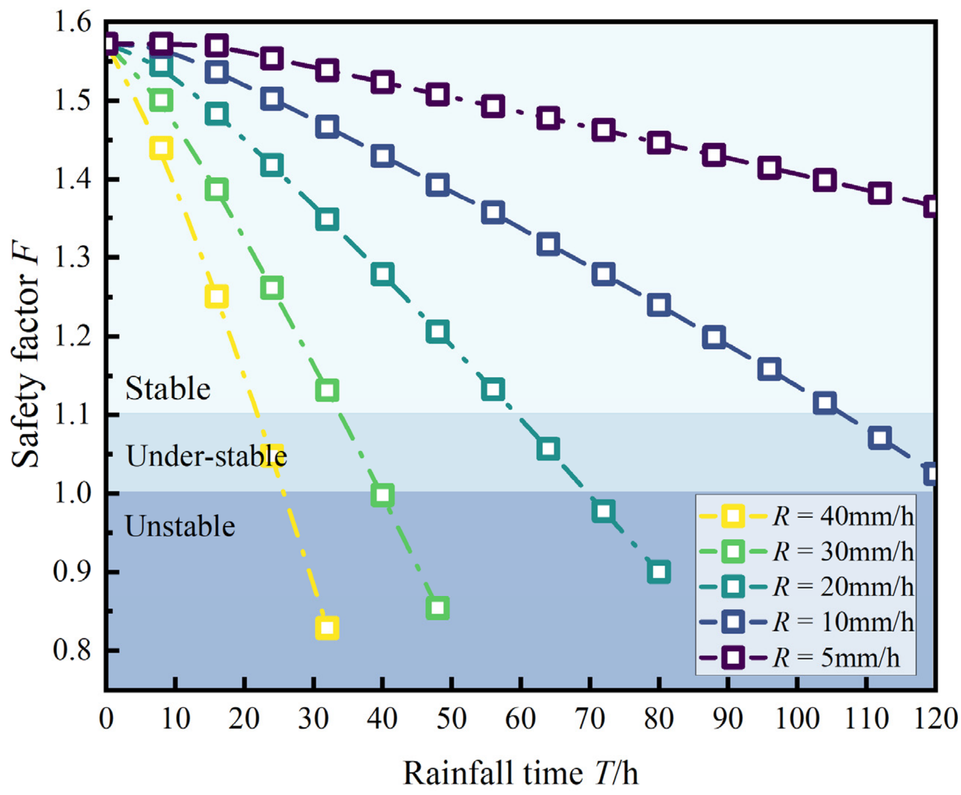

Figure 21. Change trend of safety factors.

According to the rule that the safety factor of landslide changes with rainfall time, the critical time points of landslide under-stable and unstable are obtained, and the early warning curve of landslide under rainfall conditions is established [40]. Regression analysis is carried out on the critical point of landslide stability state change under different rainfall intensities using the exponential function to obtain the landslide R-T early warning curve, as shown in Figure 22.

The rainfall warning formula for under-stable is:

$$T = 191.728 \times 0.936^{R} + 7.929 \tag{1}$$

The rainfall warning formula for unstable is:

$$T = 225.508 \times 0.936^{R} + 9.699 \tag{2}$$

In the formula, T is rainfall duration in hours; R is the rainfall intensity in mm/h. The correlation coefficients R^2 are all greater than 0.999, indicating that the regression analysis is reliable.

In the actual process of a fully weathered granite landslide warning, the slope is in danger of instability when the R-T point is above the unstable curve. When the R-T point is below the under-stable curve, the slope is safe, which can effectively warn the landslide.

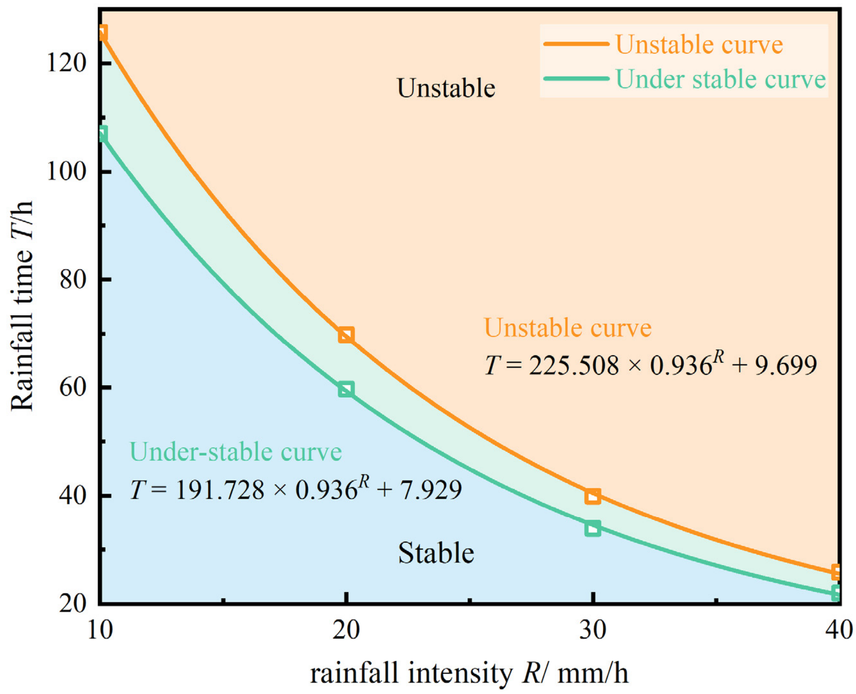

Figure 22. Warning curve of rainfall-induced fully weathered granite landslide.

5. Conclusions

To clarify the mechanism of rainfall-induced fully weathered granite landslides and establish effective warning methods, the Fanling fully weathered granite landslide is taken as the research object in this paper. Based on the physical model test, ABAQUS is used to establish the fluid–solid coupling numerical model under five different rainfall conditions. A study was conducted on the seepage field, deformation response, and stability of the slope, and the impact of rainfall intensity and time on the slope was analyzed. The main conclusions were as follows:

(1) The fully weathered granite landslide in Fanling is a pushover-type failure. The deformation occurs from the middle of the slope and extends in both directions at the bottom and top, with a faster expansion rate towards the top. And the response of horizontal deformation is greater than that of vertical deformation.

(2) The impact of different rainfall intensities and times on slope stability varies. For a completely weathered granite landslide, a short-term heavy rainstorm is more harmful than a long-term small rainstorm; the pore pressure and displacement response of the slope is faster, the loss of factor of safety of the slope is more, and the slope is more prone to instability and failure.

(3) A rainfall warning curve for under-stable and unstable of fully weathered granite landslides has been established. In future research, the author will further utilize machine learning methods to develop warning programs, providing a reference for the warning and prevention of similar regional landslides.

Author Contributions: Conceptualization, J.D. and P.Y.; formal analysis, H.L. and H.Y.; data curation, Y.X. and Y.Y.; writing—original draft preparation, P.Y. and H.L.; writing—review and editing, J.D. and P.Y.; visualization, C.Z. and Y.G.; project administration, Y.G; funding acquisition, J.D. and Y.G. All authors have approved the final manuscript. All authors have read and agreed to the published version of the manuscript.

Funding: This research was funded by the Scientific Research Fund Project of the Qingdao Geo-Engineering Surveying Institute (grant no. 2022-QDDZYKY06) and the Shandong Provincial Bureau of Geology and Mineral Resources (grant no. KY202223).

Institutional Review Board Statement: Not applicable.

Informed Consent Statement: Not applicable.

Data Availability Statement: The data presented in this study are available on request from the corresponding author.

Conflicts of Interest: The authors declare no conflict of interest.

References

1. Ministry of Natural Resources of the People's Republic of China. Available online: http://news.mnr.gov.cn/dt/mtsy/202304/t20230413_2781443.html (accessed on 13 April 2023).
2. Fan, X.; Yang, F.; Subramanian, S.S.; Xu, Q.; Feng, Z.; Mavrouli, O.; Peng, M.; Ouyang, C.; Jansen, J.D.; Huang, R. Prediction of a multi-hazard chain by an integrated numerical simulation approach: The Baige landslide, Jinsha River, China. *Landslides* **2020**, *17*, 147–164. [CrossRef]
3. Wang, M.; Shen, W.; Liu, J.; Shao, J. Phase-field modeling of cracking process in partially saturated porous media and application to rainfall-induced landslides. *Eng. Geol.* **2022**, *310*, 106884. [CrossRef]
4. Gatto, M.P.A.; Montrasio, L. X-SLIP: A SLIP-based multi-approach algorithm to predict the spatial–temporal triggering of rainfall-induced shallow landslides over large areas. *Comput. Geotech.* **2023**, *154*, 105175. [CrossRef]
5. Bao, Y.; Su, L.; Chen, J.; Ouyang, C.; Yang, T.; Lei, Z.; Li, Z. Dynamic process of a high-level landslide blocking river event in a deep valley area based on FDEM-SPH coupling approach. *Eng. Geol.* **2023**, *319*, 107108. [CrossRef]
6. Liu, X.; Wang, Y. Probabilistic simulation of entire process of rainfall-induced landslides using random finite element and material point methods with hydro-mechanical coupling. *Comput. Geotech.* **2021**, *132*, 103989. [CrossRef]
7. Li, D.; Nian, T.; Tiong, R.L.K.; Shen, Y.; Shao, Z. River blockage and impulse wave evolution of the Baige landslide in October 2018: Insights from coupled DEM-CFD analyses. *Eng. Geol.* **2023**, *321*, 107169. [CrossRef]
8. Jiang, S.; Li, J.; Zhang, S.; Gu, Q.; Lu, C.; Liu, H. Landslide risk prediction by using GBRT algorithm: Application of artificial intelligence in disaster prevention of energy mining. *Process Saf. Environ. Prot.* **2022**, *166*, 384–392. [CrossRef]
9. Sun, P.; Wang, H.; Wang, G.; Li, R.; Zhang, Z.; Huo, X. Field model experiments and numerical analysis of rainfall-induced shallow loess landslides. *Eng. Geol.* **2021**, *295*, 106411. [CrossRef]
10. Luo, S.-L.; Huang, D.; Peng, J.-B.; Aierken, A.; Li, Z.; Kuang, X.-B.; Tomás, R. Performance and application of a novel drainage anti-slide pile on accumulation landslide with a chair-like deposit-bedrock interface in the Three Gorges Reservoir area, China. *Comput. Geotech.* **2023**, *155*, 105199. [CrossRef]
11. Ji, J.; Zhang, T.; Cui, H.; Yin, X.; Zhang, W. Numerical investigation of post-earthquake rainfall-induced slope instability considering strain-softening effect of soils. *Soil Dyn. Earthq. Eng.* **2023**, *171*, 107938. [CrossRef]
12. Mreyen, A.-S.; Donati, D.; Elmo, D.; Donze, F.V.; Havenith, H.-B. Dynamic numerical modelling of co-seismic landslides using the 3D distinct element method: Insights from the Balta rockslide (Romania). *Eng. Geol.* **2022**, *307*, 106774. [CrossRef]
13. Liu, C.; Yan, Y.P.; Yang, H.Q. Numerical modeling of small-scale unsaturated soil slope subjected to transient rainfall. *Geosyst. Geoenviron.* **2023**, *2*, 100193. [CrossRef]
14. Chen, X.; Zhang, L.; Zhang, L.; Zhou, Y.; Ye, G.; Guo, N. Modelling rainfall-induced landslides from initiation of instability to post-failure. *Comput. Geotech.* **2021**, *129*, 103877. [CrossRef]
15. Yu, H.; Li, C.; Zhou, J.-Q.; Chen, W.; Zhu, Y. A semi-analytical model for transient infiltration into inclined soil interlayer considering varying water head and stratified water content. *J. Hydrol.* **2022**, *614*, 128627. [CrossRef]
16. Thomas, J.; Gupta, M.; Prusty, G. Assessing global parameters of slope stability model using Earth data observations for forecasting rainfall—Induced shallow landslides. *J. Appl. Geophys.* **2023**, *212*, 104994. [CrossRef]
17. Bilal, M.; Xing, A.; Zhuang, Y.; Zhang, Y.; Jin, K.; Zhu, Y.; Leng, Y. Coupled 3D numerical model for a landslide-induced impulse water wave: A case study of the Fuquan landslide. *Eng. Geol.* **2021**, *290*, 106209. [CrossRef]
18. Marotti, J.C.; Gomes, G.J.; Velloso, R.Q.; Júnior, E.A.V.; Nunes, R.S.; Fernandes, N.F. Exploring extreme rainfall-triggered landslides using 3D unsaturated flow, antecedent moisture and spatially distributed soil depth. *Catena* **2023**, *229*, 107241. [CrossRef]
19. Kafle, L.; Xu, W.-J.; Zeng, S.-Y.; Nagel, T. A numerical investigation of slope stability influenced by the combined effects of reservoir water level fluctuations and precipitation: A case study of the Bianjiazhai landslide in China. *Eng. Geol.* **2022**, *297*, 106508. [CrossRef]
20. Xu, J.W.; Ueda, K.; Uzuoka, R. Numerical modeling of seepage and deformation of unsaturated slope subjected to post-earthquake rainfall. *Comput. Geotech.* **2022**, *148*, 104791. [CrossRef]
21. Li, C.; Wang, M.; Chen, F.; Coulthard, T.J.; Wang, L. Integrating the SLIDE model within CAESAR-Lisflood: Modeling the 'rainfall-landslide-flash flood' disaster chain mechanism under landscape evolution in a mountainous area. *Catena* **2023**, *227*, 107124. [CrossRef]
22. Wang, C.-H.; Fang, L.; Chang, D.T.-T.; Huang, F.-C. Back-analysis of a rainfall-induced landslide case history using deterministic and random limit equilibrium methods. *Eng. Geol.* **2023**, *317*, 107055. [CrossRef]
23. Hao, J.; Jia, P.; Wu, T.; Li, W.; Chen, J.; Yang, X.; Wu, X.; Hu, G.; Cui, K.; Zhang, M. Numerical analysis of the impacts of rainfall on permafrost-related slope stability on the Qinghai–Tibet Plateau. *J. Hydrol. Reg. Stud.* **2023**, *47*, 101439. [CrossRef]

24. Fung, K.F.; Chew, K.S.; Huang, Y.F.; Ahmed, A.N.; Teo, F.Y.; Ng, J.L.; Elshafie, A. Evaluation of spatial interpolation methods and spatiotemporal modeling of rainfall distribution in Peninsular Malaysia. *Ain Shams Eng. J.* **2022**, *13*, 101571. [CrossRef]
25. Dou, H.Q.; Wang, R.; Wang, H.; Jian, W.B. Rainfall early warning threshold and its spatial distribution of rainfall-induced landslides in China. *Rock Mech. Bull.* **2023**, 100056. [CrossRef]
26. Liu, X.; Wang, Y. Analytical solutions for annual probability of slope failure induced by rainfall at a specific slope using bivariate distribution of rainfall intensity and duration. *Eng. Geol.* **2023**, *313*, 106969. [CrossRef]
27. Wei, Z.-L.; Lü, Q.; Sun, H.-Y.; Shang, Y.-Q. Estimating the rainfall threshold of a deep-seated landslide by integrating models for predicting the groundwater level and stability analysis of the slope. *Eng. Geol.* **2019**, *253*, 14–26. [CrossRef]
28. Mandal, K.; Saha, S.; Mandal, S. Applying deep learning and benchmark machine learning algorithms for landslide susceptibility modelling in Rorachu river basin of Sikkim Himalaya, India. *Geosci. Front.* **2021**, *12*, 101203. [CrossRef]
29. Novellino, A.; Cesarano, M.; Cappelletti, P.; Di Martire, D.; Di Napoli, M.; Ramondini, M.; Sowter, A.; Calcaterra, D. Slow-moving landslide risk assessment combining Machine Learning and InSAR techniques. *Catena* **2021**, *203*, 105317. [CrossRef]
30. Wang, H.; Zhang, L.; Luo, H.; He, J.; Cheung, R. AI-powered Landslide Susceptibility Assessment in Hong Kong. *Eng. Geol.* **2021**, *288*, 106103. [CrossRef]
31. Skrzypczak, I.; Kokoszka, W.; Zientek, D.; Tang, Y.; Kogut, J. Landslide Hazard Assessment Map as an Element Supporting Spatial Planning: The Flysch Carpathians Region Study. *Remote Sens.* **2021**, *13*, 317. [CrossRef]
32. Liu, H.; Yu, P.; Lu, H.; Xie, Y.; Wang, Z.; Hao, S.; Liu, H.; Fu, Y. Experimental study on disaster mechanism of completely weathered granite landslide induced by extreme rainfall. *Geoenviron. Disasters* **2023**, *10*, 5. [CrossRef]
33. Nian, T.-K.; Wu, H.; Takara, K.; Li, D.-Y.; Zhang, Y.-J. Numerical investigation on the evolution of landslide-induced river blocking using coupled DEM-CFD. *Comput. Geotech.* **2021**, *134*, 104101. [CrossRef]
34. Fan, X.; Dufresne, A.; Whiteley, J.; Yunus, A.P.; Subramanian, S.S.; Okeke, C.A.; Pánek, T.; Hermanns, R.L.; Ming, P.; Strom, A.; et al. Recent technological and methodological advances for the investigation of landslide dams. *Earth Sci. Rev.* **2021**, *218*, 103646. [CrossRef]
35. Zhang, S.G. Research on Stability Analysis of a High Slope and Optimization Design by Anti-Slide Pile. Master's Thesis, China University of Geosciences, Beijing, China, 2017. (In Chinese)
36. Zhang, S.N. Analysis of Slope Stability and Anti-Slide Pile Optimization Based on ABAQUS. Master's Thesis, Hebei University of Engineering, Shijiazhuang, China, 2019. (In Chinese)
37. Li, Z.T. Study on the Load-Displacement Coupled Prediction Parameters and Catastrophic Dynamic Prediction Criterion of the Landslides Induced by Extreme Rainfall. Master's Thesis, Qingdao Technological University, Qingdao, China, 2013. (In Chinese)
38. Tian, Y. Study on the Law of Pile-Soil Interaction and Parameter Optimization Design of Anti Slide Pile in Accumulation Landslide. Master's Thesis, Qingdao Technological University, Qingdao, China, 2021. (In Chinese)
39. Liu, X.; Wang, Y. Quantifying annual occurrence probability of rainfall-induced landslide at a specific slope. *Comput. Geotech.* **2022**, *149*, 104877. [CrossRef]
40. Zhou, K.; Wang, H.; Liao, J.; Zhang, Y.; Chen, F.; Yang, Z. Deformation and failure mechanism of colluvial landslide under sustained rainfall-a case study of Xinzhan landslide in Tongzi County, China. *Alex. Eng. J.* **2023**, *71*, 89–103. [CrossRef]